www.sciencemag.org/content/349/6251/952/suppl/DC1

Supplementary Materials for

Quantum squeezing of motion in a mechanical resonator

E. E. Wollman, C. U. Lei, A. J. Weinstein, J. Suh, A. Kronwald,
F. Marquardt, A. A. Clerk, K. C. Schwab*

*Corresponding author. E-mail: schwab@caltech.edu

Published 28 August 2015, *Science* **349**, 952 (2015)
DOI: 10.1126/science.aac5138

This PDF file includes:

1 Theory

1.1 Linearized optomechanical Hamiltonian and quantum Langevin equations

In this section, we establish the equations of motion for our system using input-output theory. The Hamiltonian of a generic optomechanical system reads

$$\hat{H} = \hbar\omega_c \hat{a}^\dagger \hat{a} + \hbar\omega_m \hat{b}^\dagger \hat{b} - \hbar g_0 \hat{a}^\dagger \hat{a} \left(\hat{b} + \hat{b}^\dagger\right) + \hat{H}_{\text{drive}}, \tag{S.1}$$

where $\hat{a}$ $\left(\hat{a}^\dagger\right)$ is the annihilation (creation) operator of the intra-cavity field, $\hat{b}$ $\left(\hat{b}^\dagger\right)$ is the mechanical phonon annihilation (creation) operator, and g_0 is the bare optomechanical coupling between the cavity and the mechanical oscillator. $\hat{H}_{\text{drive}}$ describes the external driving.

In our experiment, the optomechanical system consists of an electromechanical system with two ports. We drive the cavity mode with two microwave tones from the left port, which we designate (L). The drive Hamiltonian reads

$$\hat{H}_{\text{drive}} = \hbar \sum_{\nu=\pm} \alpha_\nu \left(\hat{a} e^{i\omega_\nu t} + \hat{a}^\dagger e^{-i\omega_\nu t}\right), \tag{S.2}$$

where $\omega_\pm = \omega_c + \Delta \pm (\omega_m + \delta)$ and $\alpha_\pm$ are the blue and red pump amplitudes at the input port. The detunings δ and Δ are shown in Fig. SS1. In the following, we apply standard linearization – i.e., we separate the cavity and the mechanical operators, $\hat{a}$ and $\hat{b}$, into a classical part, $\bar{a}$ or $\bar{b}$, plus quantum fluctuations, $\hat{d}$ or $\hat{c}$. E.g., $\hat{a} \to \bar{a} + \hat{d}$. In the interaction picture with respect to $\hat{H}_0 = \hbar\left(\omega_c + \Delta\right)\hat{a}^\dagger\hat{a} + \hbar\left(\omega_m + \delta\right)\hat{b}^\dagger\hat{b}$, we find the *linearized* optomechanical Hamiltonian

$$\hat{H}_{\text{lin}} = \hat{H}_{\text{RWA}} + \hat{H}_{\text{CR}}\,. \tag{S.3}$$

Here,

$$\hat{H}_{\text{RWA}} = -\hbar\Delta\hat{d}^\dagger\hat{d} - \hbar\delta\hat{c}^\dagger\hat{c} - \hbar\left[\left(G_+\hat{c}^\dagger + G_-\hat{c}\right)\hat{d}^\dagger + \left(G_+\hat{c} + G_-\hat{c}^\dagger\right)\hat{d}\right] \tag{S.4}$$

describes the resonant part of the linearized optomechanical interaction whereas

$$\hat{H}_{\text{CR}} = -\hbar\left[G_+ e^{-2i(\omega_m+\delta)t}\hat{c} + G_- e^{2i(\omega_m+\delta)t}\hat{c}^\dagger\right]\hat{d}^\dagger - \hbar\left[G_+ e^{2i(\omega_m+\delta)t}\hat{c}^\dagger + G_- e^{-2i(\omega_m+\delta)t}\hat{c}\right]\hat{d} \tag{S.5}$$

describes off-resonant optomechanical interactions. Note that $G_\pm = g_0\bar{a}_\pm$ describes the driven-enhanced optomechanical coupling. Here, $\bar{a}_\pm$ is the intracavity microwave amplitude due to the red and blue pumps, and we have assumed $\bar{a}_\pm \in \mathbb{R}$ for simplicity and without loss of generality.

Let us first consider the good cavity limit $(\omega_m \gg \kappa)$. We will later discuss how to incorporate corrections due to bad cavity effects in Section 1.4. This allows us to work within the rotating wave approximation. Thus, $\hat{H}_{\text{lin}} \approx \hat{H}_{\text{RWA}}$. In that case, the linearized quantum Langevin equations read

$$\dot{\hat{d}} = -\left(\frac{\kappa}{2} - i\Delta\right)\hat{d} + i\left(G_-\hat{c} + G_+\hat{c}^\dagger\right) + \sqrt{\kappa}\hat{d}_{\text{in}}, \tag{S.6}$$

$$\dot{\hat{c}} = -\left(\frac{\gamma_m}{2} - i\delta\right)\hat{c} + i\left(G_-\hat{d} + G_+\hat{d}^\dagger\right) + \sqrt{\gamma_m}\hat{c}_{\text{in}}\,. \tag{S.7}$$

Here, $\hat{d}_{\text{in}} = \sum_{\sigma=L,R,I} \sqrt{\frac{\kappa_\sigma}{\kappa}} \hat{d}_{\sigma,\text{in}}$ is the total input noise of the cavity, where $\hat{d}_{\sigma,\text{in}}$ describes the input fluctuations to the cavity from channel σ with damping rate κ_σ. $\sigma = L$ and R correspond to the left and right microwave cavity ports, while $\sigma = I$ corresponds to internal losses. The noise operator $\hat{c}_{\text{in}}$ describes quantum and thermal noise of the mechanical oscillator with intrinsic damping rate γ_m. The input field operators satisfy the following commutation relations:

$$\left[\hat{d}_{\sigma,\text{in}}(t), \hat{d}^\dagger_{\sigma',\text{in}}(t')\right] = \delta_{\sigma,\sigma'}\delta(t-t'), \tag{S.8}$$

$$\left[\hat{c}_{\text{in}}(t), \hat{c}^\dagger_{\text{in}}(t')\right] = \delta(t-t'), \tag{S.9}$$

$$\left\langle \hat{d}^\dagger_{\sigma',\text{in}}(t)\, \hat{d}_{\sigma,\text{in}}(t') \right\rangle = n^{\text{th}}_\sigma \delta_{\sigma,\sigma'}\delta(t-t'), \tag{S.10}$$

$$\left\langle \hat{c}^\dagger_{\text{in}}(t)\, \hat{c}_{\text{in}}(t') \right\rangle = n^{\text{th}}_m \delta(t-t'), \tag{S.11}$$

where n^{th}_σ is the photon occupation in port σ, and $n^{\text{th}}_m = 1/\left[\exp\left(\hbar\omega_m/k_B T\right) - 1\right]$ is the thermal occupation of the mechanical oscillator. The total occupation of the cavity is the weighted sum of the contributions from different channels: $n^{\text{th}}_c = \sum_\sigma \frac{\kappa_\sigma}{\kappa} n^{\text{th}}_\sigma$.

1.2 Optomechanical output spectrum and mechanical spectrum

In this section, we derive the optomechanical output spectrum and the mechanical quadrature spectrum, first within the RWA and later in Sec. 1.3 including bad cavity effects. For this, we solve the quantum Langevin equations (Eqs. S.6, S.7) in Fourier space. It is convenient to define the vectors $\boldsymbol{D} = \left(\hat{d}, \hat{d}^\dagger, \hat{c}, \hat{c}^\dagger\right)^T$, $\boldsymbol{D}_{\text{in}} = \left(\hat{d}_{\text{in}}, \hat{d}^\dagger_{\text{in}}, \hat{c}_{\text{in}}, \hat{c}^\dagger_{\text{in}}\right)^T$ and $\boldsymbol{L} = \text{diag}\left(\sqrt{\kappa}, \sqrt{\kappa}, \sqrt{\gamma_m}, \sqrt{\gamma_m}\right)$. We then find the following solution to the quantum Langevin equations in frequency space:

$$\hat{\boldsymbol{D}}[\omega] = \boldsymbol{\chi}[\omega] \cdot \boldsymbol{L} \cdot \hat{\boldsymbol{D}}_{\text{in}}[\omega], \tag{S.12}$$

where

$$\boldsymbol{\chi}[\omega] \equiv \begin{pmatrix} \frac{\kappa}{2} - i(\omega+\Delta) & 0 & -iG_- & -iG_+ \\ 0 & \frac{\kappa}{2} - i(\omega-\Delta) & iG_+ & iG_- \\ -iG_- & -iG_+ & \frac{\gamma_m}{2} - i(\omega+\delta) & 0 \\ iG_+ & iG_- & 0 & \frac{\gamma_m}{2} - i(\omega-\delta) \end{pmatrix}^{-1}. \tag{S.13}$$

We measure the output light spectrum through the undriven (right) cavity port. One finds the output light field $\hat{d}_{R,\text{out}}(\omega)$ using the input-output relation $\hat{d}_{\sigma,\text{out}}(\omega) = \hat{d}_{\sigma,\text{in}}(\omega) - \sqrt{\kappa_\sigma}\hat{d}(\omega)$. This yields

$$\hat{d}_{R,\text{out}}(\omega) = \hat{d}_{R,\text{in}}(\omega) - \sqrt{\kappa_R\kappa}\left(\boldsymbol{\chi}[\omega]\right)_{11}\hat{d}_{\text{in}} - \sqrt{\kappa_R\kappa}\left(\boldsymbol{\chi}[\omega]\right)_{12}\hat{d}^\dagger_{\text{in}} \tag{S.14}$$

$$- \sqrt{\kappa_R\gamma_m}\left(\boldsymbol{\chi}[\omega]\right)_{13}\hat{c}_{\text{in}} - \sqrt{\kappa_R\gamma_m}\left(\boldsymbol{\chi}[\omega]\right)_{14}\hat{c}^\dagger_{\text{in}}. \tag{S.15}$$

The transmission spectrum (driven response) is given by

$$T[\omega] = -\sqrt{\kappa_L\kappa_R}\left(\boldsymbol{\chi}[\omega]\right)_{11}. \tag{S.16}$$

For our system, $n^{\text{th}}_R = 0$, so the symmetric noise spectral density is given by

$$\bar{S}_R[\omega] = \frac{1}{2}\int dt \left\langle \left\{ \hat{d}^\dagger_{R,\text{out}}[0], \hat{d}_{R,\text{out}}[t] \right\} \right\rangle e^{i\omega t} = \frac{1}{2} + S_R[\omega], \tag{S.17}$$

where

$$\begin{aligned} S_R[\omega] &= \frac{1}{2}\int dt \left\langle \hat{d}^{\dagger}_{R,\text{out}}[0]\,\hat{d}_{R,\text{out}}[t]\right\rangle e^{i\omega t} \\ &= \kappa_R\kappa\left|(\boldsymbol{\chi}[\omega])_{11}\right|^2 n_{\text{c}}^{\text{th}} + \kappa_R\kappa\left|(\boldsymbol{\chi}[\omega])_{12}\right|^2\left(n_c^{\text{th}}+1\right) \\ &\quad +\kappa_R\gamma_m\left|(\boldsymbol{\chi}[\omega])_{13}\right|^2 n_m^{\text{th}} + \kappa_R\gamma_m\left|(\boldsymbol{\chi}[\omega])_{14}\right|^2\left(n_m^{\text{th}}+1\right), \end{aligned} \tag{S.18}$$

For $\delta = 0$, the expressions can be simplified to

$$T[\omega] = -\frac{2\sqrt{\kappa_L\kappa_R}\left(\gamma_m - 2i\omega\right)}{4G^2 + \left[\kappa - 2i\left(\omega+\Delta\right)\right]\left(\gamma_m - 2i\omega\right)}, \tag{S.19}$$

$$S_R(\omega) = \kappa_R\frac{4\gamma_m\left[\gamma_m\kappa n_{\text{c}}^{\text{th}} + 4G_-^2 n_m^{\text{th}} + 4G_+^2\left(n_m^{th}+1\right)\right] + 16\kappa n_{\text{c}}^{\text{th}}\omega^2}{\left|4G^2 + \left(\kappa+2i\omega\right)\left[\gamma_m + 2i\left(\omega+\Delta\right)\right]\right|^2}, \tag{S.20}$$

where $G^2 = G_-^2 - G_+^2$. For both $\delta = 0$ and $\Delta = 0$, the mechanical quadrature spectra are

$$\begin{aligned} \bar{S}_{X_{1,2}}[\omega] &= \frac{1}{2}\int dt \left\langle\left\{\hat{X}_{1,2}(t), \hat{X}_{1,2}(0)\right\}\right\rangle e^{i\omega t} \\ &= 4x_{zp}^2\frac{4\kappa\left(G_- \mp G_+\right)^2\left(n_{\text{c}}^{\text{th}}+\frac{1}{2}\right) + \gamma_m\left(\kappa^2+4\omega^2\right)\left(n_m^{\text{th}}+\frac{1}{2}\right)}{\left[4G^2+\gamma_m\kappa\right]^2 + 4\left(\gamma_m^2+\kappa^2-8G^2\right)\omega^2 + 16\omega^4}. \end{aligned} \tag{S.21}$$

The mechanical quadrature fluctuations are obtained by integrating the mechanical quadrature spectra

$$\begin{aligned} \left\langle \hat{X}_{1,2}^2\right\rangle &= \int\frac{d\omega}{2\pi}\bar{S}_{X_{1,2}}(\omega) \\ &= x_{zp}^2\frac{4\left(G_- \mp G_+\right)^2\kappa\left(2n_{\text{c}}^{\text{th}}+1\right) + \left[4G^2+\kappa\left(\kappa+\gamma_m\right)\right]\gamma_m\left(2n_m^{\text{th}}+1\right)}{\left(\kappa+\gamma_m\right)\left(4G^2+\kappa\gamma_m\right)}, \end{aligned} \tag{S.22}$$

1.3 Mechanical spring constant and resonance frequency

In this section, we confirm that the interaction with the cavity does not appreciably modify the mechanical frequency and spring constant; this then confirms that the zero-point position variance $x_{\text{zp}} = \sqrt{\hbar\omega_m/2k}$ is also not changed. Starting from the solution to the quantum Langevin equations in frequency space, we express the mechanical operator equation using the terms of the scattering parameters,

$$\hat{c} = \boldsymbol{\chi}_{31}\sqrt{\kappa}\hat{d}_{\text{in}} + \boldsymbol{\chi}_{32}\sqrt{\kappa}\hat{d}_{\text{in}}^{\dagger} + \boldsymbol{\chi}_{33}\sqrt{\gamma_m}\hat{c}_{\text{in}} + \boldsymbol{\chi}_{34}\sqrt{\gamma_m}\hat{c}_{\text{in}}^{\dagger}, \tag{S.23}$$

where all explicit frequency dependence has been omitted. In this notation, the mechanical susceptibility is given by the scattering factor $\boldsymbol{\chi}_{33}$. In Fig. S5, we plot the mechanical density of states both with and without the optomechanical interaction.

We also explicitly calculate the change in the mechanical frequency due to the interaction with the cavity by looking at the corresponding "self energy" (i.e. difference in inverse mechanical susceptibilities with and without the cavity, see e.g. (*19*)). With the system parameters taken at

optimal squeezing, the interaction with the cavity alters the resonance frequency by a factor of 10^{-3}.

Having confirmed that the mechanical resonance frequency is almost unaltered, we next consider the change in the mechanical spring constant, i.e. the response of the mechanical position to a DC force. We take the average of Eq. S.23, setting the average of $\sqrt{\gamma_m}\hat{c}_{\rm in} = -iFx_{\rm zp}/\hbar$, where F represents a DC classical force. Solving for position at zero frequency in the lab frame,

$$\langle \hat{x}\,[0]\rangle = \frac{2Fx_{\rm zp}^2}{\hbar}\{{\rm Im}(\boldsymbol{\chi}_{33}\,[0]) - {\rm Im}(\boldsymbol{\chi}_{34}\,[0])\}.$$

The spring constant k is defined in terms of the position and force terms from above, $\hat{x}\,[0]\,/F = 1/k$. For the mechanics absent the optomechanical interaction, $\langle \hat{x}\,[0]\rangle/F = 1/(m\omega_m^2)$ as expected. Including the optomechanical interaction and taking parameters corresponding to the optimal squeezing generation, we find that $\langle \hat{x}\,[0]\rangle/F$ is modified by 0.1%.

We have now shown that the both the spring constant and mechanical resonance frequency differs by a factor of 10^{-3} when the optomechanical interaction is taken into account. The behavior of the mechanics is insignificantly modified by the strong microwave pumps implying that there is no modification of the zero-point scale.

1.4 Calculation of bad cavity effects on the amount of squeezing

In the previous sections, we have focused on the good cavity limit where $\kappa/\omega_m \ll 1$, such that spurious off-resonant interactions described by $\hat{H}_{\rm CR}$ (cf. Eq. (S.5)) have been omitted. In this section, we briefly comment on how to include bad cavity effects. As already mentioned, these can become important if the sideband parameter $\kappa/\omega_m \not\ll 1$ and possibly alter the lineshape of the microwave noise spectrum or degrade the amount of mechanical squeezing. For our devices, $\kappa/\omega_m \sim 1/8$, so the bad cavity effects are small, but not negligible.

In the frequency domain, the explicit time-dependence of $\hat{H}_{\rm CR}$ couples system operators at different frequencies to each other,

$$\hat{\boldsymbol{D}}_{\boldsymbol{CR}}\,[\omega] = \boldsymbol{\chi}_{\boldsymbol{CR}}\,[\omega]\cdot\boldsymbol{L}_{\boldsymbol{CR}}\cdot\hat{\boldsymbol{D}}_{\boldsymbol{CR},\rm in}\,[\omega]\,. \tag{S.24}$$

Here, $\hat{\boldsymbol{D}}_{\boldsymbol{CR}}\,[\omega]$ contains infinitely many sidebands detuned by $\Omega = 2\,(\omega_m+\delta)$,

$$\hat{\boldsymbol{D}}_{\boldsymbol{CR}}[\omega] = \Big(...\;\hat{\boldsymbol{D}}[\omega-2\Omega],\;\hat{\boldsymbol{D}}[\omega-\Omega],\;\hat{\boldsymbol{D}}[\omega],\;\hat{\boldsymbol{D}}[\omega+\Omega],\;\hat{\boldsymbol{D}}[\omega+2\Omega]\;...\Big)\,,$$

while $\hat{\boldsymbol{D}}\,[\omega]$ is defined in the same manner as in Sec. 1.2. Note that we do not report $\boldsymbol{\chi}_{\boldsymbol{CR}}$ or $\boldsymbol{L}_{\boldsymbol{CR}}$ as these large matrices are not very enlightening. In order to solve the equations of motion, we truncate the number of sidebands that we take into account, i.e. we truncate the length of $\hat{\boldsymbol{D}}_{\boldsymbol{CR}}$ to the $n^{\rm th}$ sideband at frequency $(\omega_m \pm n\Omega)$. As the analytic solutions are unwieldy even for first order corrections, we instead numerically calculate the spectrum at frequencies specified by the data.

Similarly, the mechanical quadrature spectra $\bar{S}_{X_{1,2}}$ can be calculated including bad cavity effects. Again, we numerically derive the spectra then extract $\langle X_{1,2}^2\rangle = \int \frac{d\omega}{2\pi}\bar{S}_{X_{1,2}}$ via numerical integration over a span 2000 times the total mechanical linewidth.

2 Device fabrication

We start with a 525 μm thick <100>-oriented high resistivity (>10 k$\Omega\cdot$ cm) silicon wafer. After initial surface preparation, a 100 nm layer of aluminum is DC magnetron sputtered in a UHV chamber with base pressure of $\sim 10^{-9}$ Torr. The bottom layer is patterned via contact photolithography followed by two-step wet etching in Transene Al Etchant A and MF-319. Next, we spin and pattern S1813 which acts as a sacrificial layer in the capacitor gap and a protection layer for the rest of the bottom layer pattern. In order to thin down the sacrificial layer, we flood expose the S1813 prior to development. Before processing the top aluminum layer, we use a short O_2 plasma etch to increase adhesion between the sacrificial and top layer. A 100 nm aluminum layer is sputtered and patterned under the same procedure for the bottom layer. The resulting device is cleaned and released in an overnight soak in Remover-PG followed by critical point drying and a final short O_2 plasma clean.

3 Measurements

3.1 Initial calibration measurements

We begin by performing two measurements that calibrate the pump powers detected at the output of our measurement chain, $P_\pm = gain \times \hbar\omega_\pm \times \kappa_R \Delta_\pm n_p^\pm$, in terms of enhanced optomechanical coupling rates, $G_\pm$, as well as the effective intracavity photon levels, $\Delta_\pm n_p^\pm$. Here, $\Delta_\pm$ is a correction factor that modifies the cavity transmission off resonance (*29*) and has no significance in the following analysis.

With scanning homodyne detection (i.e., via a driven response), we first measure the mechanical linewidth, $\gamma_{\rm tot} = \gamma_m + \gamma_{\rm opt}$, as we increase the power, P_-, of a single pump red-detuned from the cavity center by ω_m. Here, $\gamma_{\rm opt} = 4G_-^2/\kappa$ is the optically-induced mechanical damping. When $\gamma_{\rm tot}$ is much less than κ, the mechanical response is a simple Lorentzian dip (Fig. S2A). In this regime, we fit $\gamma_{\rm opt}$ vs. $P_\pm$ to obtain a calibration for G_-^2, as seen in Fig. 2B. When $\gamma_{\rm tot}$ becomes comparable to κ, the cavity experiences mode-splitting, and a Lorentzian model can no longer describe the mechanical response (Fig. S2B). We thus fit Eq. S.19 to the transmission, with $G_+ = 0$ and $\delta = 0$. The values of G_- extracted from the fit to the full model is in good agreement with the linear fit to $\gamma_{\rm opt}$ at lower powers, as seen in Fig. S3.

Next, we place two balanced pumps, detuned from cavity center by $\pm(\omega_m + 2\pi \times 500\,{\rm Hz})$ and with powers $P_\pm$, at sufficiently low powers so as not to add any damping or amplification of the thermal noise, and we measure the integrated mechanical noise power of up- and down-converted motional sidebands, $P_m^\pm$, over a range of cryostat temperatures T. Due to weak temperature and power dependence of κ (*21*), we monitor the cavity linewidth at each measurement power or temperature. The results of these calibrations are cast in a linear form and fit with ordinary least squares to extract the calibration factors a, b_- and b_+,

$$\left(\frac{\kappa}{\bar{\kappa}}\right)\gamma_{\rm opt} = \frac{4G_-^2}{\bar{\kappa}} = a\left(\frac{4}{\bar{\kappa}}\right)P_-, \tag{S.25}$$

$$\left(\frac{\kappa}{\bar{\kappa}}\right)^2 \frac{P_m}{P_\pm} = b_\pm \left(\frac{2}{\bar{\kappa}}\right)^2 \frac{k_B T}{\hbar\omega_m}, \tag{S.26}$$

where $\bar{\kappa}$ is the cavity linewidth averaged over the respective parameter range. We find

$$a = (3.25 \pm 0.09) \times 10^{16}\,\mathrm{rad^2\,s^{-2}\,W^{-1}},$$
$$b_- = (3.82 \pm 0.14) \times 10^{4}\,\mathrm{rad^2\,s^{-2}},$$
$$b_+ = (6.84 \pm 0.22) \times 10^{4}\,\mathrm{rad^2\,s^{-2}}.$$

We now are able to formulate the pump-dependent model parameters in terms of $P_\pm$,

$$G_-^2 = a \times P_-, \tag{S.27}$$
$$G_+^2 = a\left(\frac{b_-}{b_+}\right) \times P_+, \tag{S.28}$$
$$\Delta_- n_p^- = \left(\frac{a}{b_-}\right) \times P_-. \tag{S.29}$$

Eq. (S.28) follows from the balancing condition $\left(\frac{P_-}{P_+}\right)_{\text{balanced}} = \left(\frac{b_-}{b_+}\right)$.

3.2 Noise spectrum measurement

We first measure the complex transmission through the system at each reported power ratio. Setting the enhanced optomechanical coupling rates via Eqs. (S.27-S.29), we fit the transmission spectrum to Eq. (S.19) via nonlinear least squares estimation and extract the frequency of the microwave resonator ω_c, the cavity linewidth κ, the frequency of the mechanical oscillator ω_m, and the pump detunings Δ, δ. The two pump tones are iteratively aligned to overlap the mechanical sidebands at the center of the cavity to ensure that δ is close to 0 (Fig. S4).

We then measure the microwave noise spectrum via linear detection, keeping the same two-tone pump configuration as above. The measured spectrum is given by

$$\bar{S}_{\text{out}}(\omega) = S_0(\omega) + S_R(\omega), \tag{S.30}$$

where $S_R(\omega)$ is the noise spectrum of the electro-mechanical system and $S_0(\omega)$ is the noise floor of the system. The noise floor is dominated by the noise figure of the cryogenic HEMT amplifier in addition to smaller power-dependent offsets due to phase noise from the entire amplifier chain. We spend an equal time interleaving measurements of the pumped and unpumped noise spectra over the same bandwidth. We subtract off the unpumped floor, then account for power-dependent amplifier effects by removing a linear floor offset that we fit over a span ~ 7 times greater than the cavity linewidth. The linear offset matches independent measurements of the phase noise from our room temperature amplifier with matching pump configuration.

4 Error analysis and fitting of the output spectrum

Essential to any claim of sub-zero-point squeezing is the error bar for the reported quadrature occupation. Here, we consider a systematic approach to incorporate the uncertainty from all the sources of our measurement, including systematic calibration error, measurement noise, and the uncertainty from fitting the model to a measured noise spectrum. This problem has been addressed

by Bayesian analysis techniques that explicitly incorporate all known sources of error. In the following, we largely follow the analysis outlined in Ch. 3 of (*30*). Our purpose for using this analysis is to address the issue of estimating error bars from nonlinear fitting with a fit model that also has uncertainty.

In what follows, we develop statistical estimators for the quadrature occupations, $\langle X_{1,2}^2 \rangle$, from two sets of measurements: the detected noise spectrum and the system calibrations. Here, system calibration refers to the combination of initial calibrations (a, b_-, b_+), driven response data (κ, Δ, δ) and power detection (P_-, P_+). We refer to such parameters as $\beta = \{a, b_-, b_+, \kappa, \Delta, \delta, P_-, P_+\}$. The only remaining unknowns are the bath contributions, here denoted as $\alpha = \{n_c^{\mathrm{th}}, \gamma_m n_m^{\mathrm{th}}\}$.

To systematically incorporate the uncertainty from our calibrations and spectrum measurements, we consider the Bayesian posterior distribution

$$p\left(\alpha, \beta | D, I\right) = \frac{1}{Z} p\left(D | \alpha, \beta, I\right) p\left(\alpha, \beta\right), \tag{S.31}$$

where D is the observed noise data, I is the set of all assumptions required for this analysis, $Z = p\left(D\right)$ is a normalization constant that is not necessary for sampling of the posterior, $p\left(D|\alpha, \beta, I\right)$ is the likelihood function, and $p\left(\alpha, \beta\right)$ is the prior distribution for α, β.

The prior distribution captures how well we have confined our calibrations in parameter space. Assuming all system parameters are independent, the prior simplifies to a product of single-parameter normal distributions, i.e. $p\left(\beta\right)$ is a product of Gaussian distributions with mean and variance set by the statistical estimators for each system calibrations. For the unknowns, $p\left(\alpha\right)$ is the product of uninformed Jeffreys priors; these priors are uniform in log space and here set to span a decade above and below initial estimates for n_c^{th}, $\gamma_m n_m^{\mathrm{th}}$.

The likelihood captures how well the data matches the noise spectrum model with specified α, β. We calculate data residuals by subtracting the full noise spectrum model, including bad-cavity effects as discussed in Sec. 1.4, from the detected noise. Next, we assume the measurement noise is independent and Gaussian distributed with constant variance. Hence, the likelihood is the product of residual probabilities derived from $N(0, \sigma)$, where σ is sampled from noise data over a 150 kHz window detuned outside cavity center by $\pm 3\kappa$.

Since the posterior distribution is difficult to calculate analytically, we instead model the posterior via an affine-invariant Markov chain Monte Carlo (MCMC) ensemble sampler (*31*). We implement this calculation with *emcee*, an open-source Python package developed in the astronomy community with over 300 citations since 2012 (*32*). With *emcee*, we generate a sufficiently large number of of pseudo-random parameter chains (α_i, β_i) sampled from the posterior distribution. For the calculation, we initialize 10^2 walkers and run for a minimum of 10^3 steps. We discard the first half to ensure that the resulting distributions are steady state (allowing initial transients to relax) but maintain large enough sample size to render the Monte Carlo uncertainty negligible.

Finally, we calculate expectation values and 1-σ intervals for n_c^{th}, $\gamma_m n_m^{\mathrm{th}}$ and $\langle X_{1,2}^2 \rangle$. For n_c^{th} and $\gamma_m n_m^{\mathrm{th}}$, we construct the marginalized distributions from their respective Markov chains and then tabulate the statistical estimators for mean and variance. For the mechanical quadratures, we calculate expectation values for functions of system parameters, $f\left(\alpha, \beta\right)$, with function evaluation

over the entire MCMC ensemble,

$$\langle f \rangle = \int f(\alpha, \beta)\, p(\alpha, \beta | D, I)\, d\alpha d\beta, \tag{S.32}$$

$$\simeq \frac{1}{N} \sum_{i=1}^{N} f(\alpha_i, \beta_i). \tag{S.33}$$

The mean and standard deviation for $\langle X_{1,2}^2 \rangle$ are generated via Eq. (S.33) with $f(\alpha, \beta)$ set to the mechanical quadrature functions discussed in Sec. 1.4.

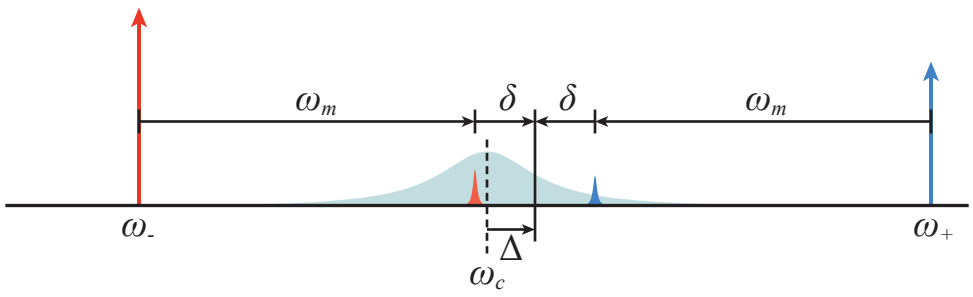

Fig. S1: Definition of detuning parameters for an optomechanical system with a two-tone drive.

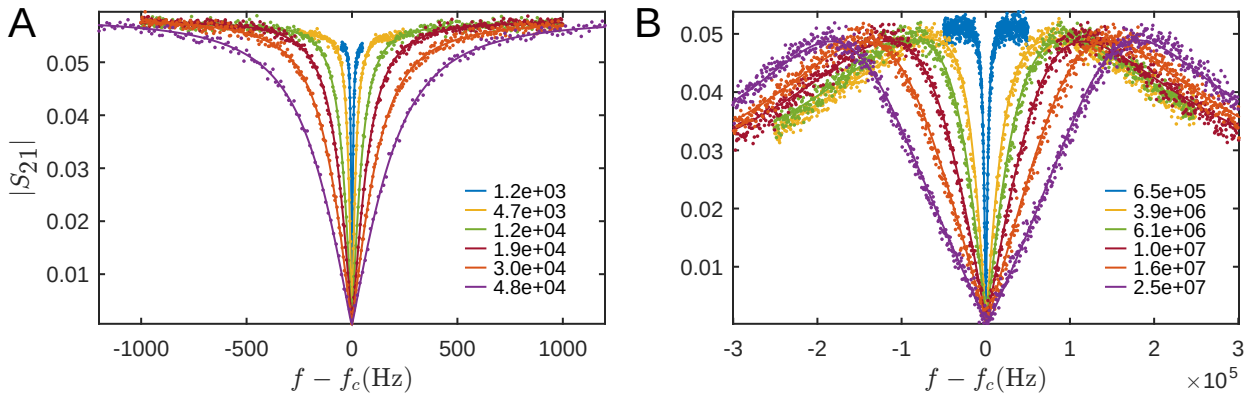

Fig. S2: Cavity transmission spectra in the presence of a microwave drive at frequency $\omega_- = \omega_c - \omega_m$. A. Transmission spectra in weak-driving regime, with n_p^- ranging from 1.2e3 to 4.8e4. In this regime, the spectrum can be described by a Lorentzian dip with an effective mechanical linewidth $\gamma_{\text{tot}} = \gamma_m + \gamma_{opt}$. Increasing the pump photon number increases the optical damping rate and broadens the mechanical signal. B. Transmission spectra in the strong-driving regime, with n_p^- ranging from 6.5e5 to 2.5e7. When the effective mechanical linewidth γ_{tot} is comparable to the cavity linewidth κ, the resonance starts to split into normal modes, which are the hybrids of the mechanical oscillations and the microwave resonance. In this regime, the full model (S.19) is used to describe the transmission spectrum.

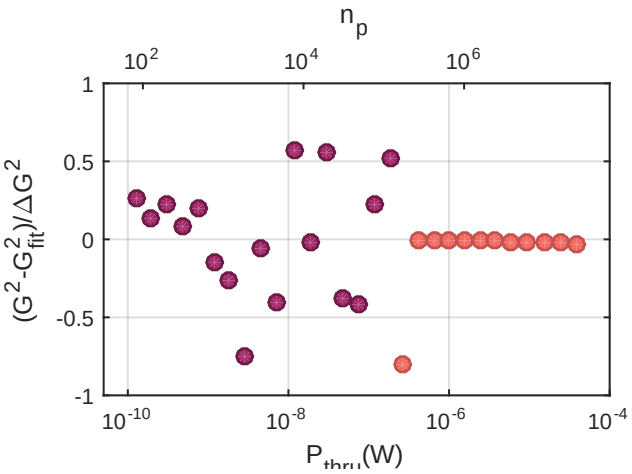

Fig. S3: Normalized residuals of the enhanced electromechanical coupling rate. Purple circles: weak-driving regime in which the mechanical susceptibility is a simple lorentzian. Red circles: strong-driving regime in which the mechanical linewidth becomes comparable to the cavity linewidth and must be extracted using a full model. The linearity of our device at high pump powers is shown by calculating the normalized residuals of these strong-driving points to the fit line from the weak-driving regime.

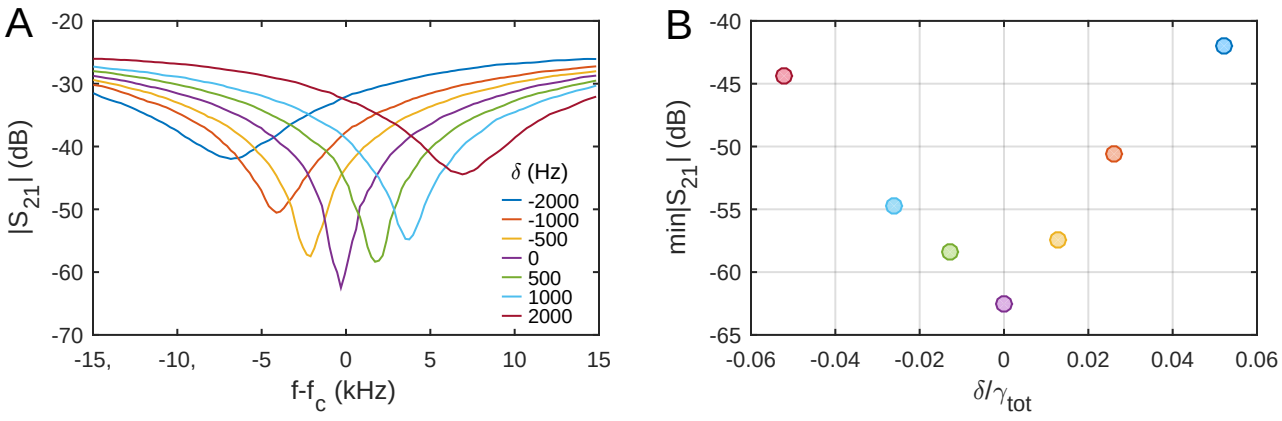

Fig. S4: Sideband alignment precision. (A) Transmission spectra in the presence of two drives at frequencies equal to $\omega_{\pm}$; the dip in the spectrum is due to the two tones' electromechanically induced transparency effect. The detuning δ is given by $\left(\omega_+ - \omega_- - 2\omega_m\right)/2$. The transmission at ω_c is minimized when the up-converted mechanical sideband from the red pump and the down-converted mechanical sideband from the blue pump are perfectly overlapped. (B) The minimum value of the transmission spectrum in (A) vs. detuning. The precision of the alignment is within a few percent of the total mechanical linewidth $\gamma_{\text{tot}} = \gamma_m + \frac{4}{\kappa}(G_-^2 - G_+^2)$.

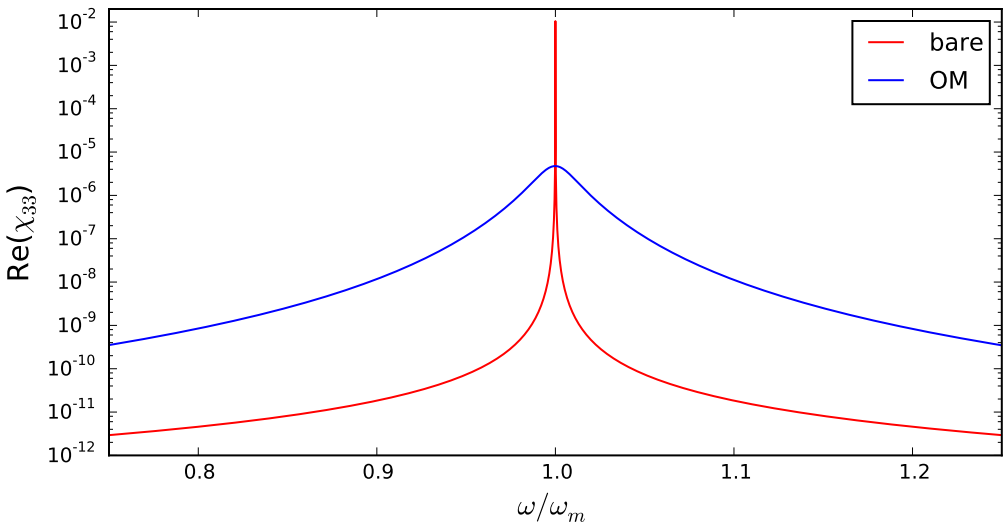

Fig. S5: The mechanical density of states, defined as $\mathrm{Re}(\chi_{33})$, both with ("OM") and without ("bare") the optomechanical interaction. At optimal squeezing parameters, the mechanics is significantly damped by the optomechanical interaction, however the location of the mechanical peak, and hence the mechanical resonance frequency, is insignificantly modified by the interaction.